JMI Journal of Medical Imaging

RESEARCH PAPER

Neodymium acetate as a contrast agent for X-ray phase-contrast tomography

Jakob Reichmann[a], **Torben Ruhwedel**[b], **Wiebke Möbius**[b] and **Tim Salditt**[a,*]

[a]Georg-August-University of Göttingen, Göttingen, Germany

[b]Max Planck Institute for Multidisciplinary Sciences, Göttingen, Germany

ABSTRACT. **Purpose:** X-ray phase-contrast tomography (XPCT) is a non-destructive, three-dimensional imaging modality that provides higher contrast in soft tissue than absorption-based CT and allows one to cover the cytoarchitecture from the centi- and millimeter scale down to the nanoscale. To further increase contrast and resolution of XPCT, for example, in view of addressing connectivity issues in the central nervous system (CNS), metal staining is indispensable. However, currently used protocols, for example, based on osmium and/or uranium are less suited for XPCT, due to an excessive β/δ-ratio. In this work, we explore the suitability of different staining agents for XPCT. Particularly, neodymium(III)-acetate (NdAc), which has recently been proposed as a non-toxic, non-radioactive easy to use alternative contrast agent for uranyl acetate (UAc) in electron microscopy, is investigated. Due to its vertical proximity to UAc in the periodic table, similar chemical but better suited optical properties for phase contrast can be expected.

Approach: Differently stained whole eye samples of wild type mouse and tissues of the CNS are embedded into EPON epoxy resin and scanned using synchrotron as well as with laboratory radiation. Phase retrieval is performed on the projection images, followed by tomographic reconstruction, which enables a quantitative analysis based on the reconstructed electron densities. Segmentation techniques and rendering software is used to visualize structures of interest in the sample.

Results: We show that staining neuronal samples with NdAc enhances contrast, in particular for laboratory scans, allowing high-resolution imaging of biological soft tissue in-house. For the example of murine retina, specifically rods and cones as well as the sclera and the Ganglion cell layer seem to be targeted by the stain. A comparison of electron density by the evaluation of histograms allowed to determine quantitative measures to describe the difference between the examined stains.

Conclusion: The results suggest NdAc to be an effective stain for XPCT, with a preferential binding to anionic groups, such as phosphate and carboxyl groups at cell surfaces, targeting certain layers of the retina with a stronger selectivity compared to other staining agents. Due to the advantageous X-ray optical properties, the stain seems particularly well-suited for phase contrast, with a comparably small number density and an overall superior image quality at laboratory sources.

© The Authors. Published by SPIE under a Creative Commons Attribution 4.0 International License. Distribution or reproduction of this work in whole or in part requires full attribution of the original publication, including its DOI. [DOI: 10.1117/1.JMI.10.5.056001]

Keywords: contrast agent; X-ray phase-contrast tomography; neodymium acetate; staining; neuroimaging; retina

Paper 22289GR received Nov. 8, 2022; revised Aug. 8, 2023; accepted Oct. 2, 2023; published Oct. 25, 2023.

*Address all correspondence to Tim Salditt, tsaldit@gwdg.de

Downloaded From: https://www.spiedigitallibrary.org/journals/Journal-of-Medical-Imaging on 11 Jan 2024
Terms of Use: https://www.spiedigitallibrary.org/terms-of-use

1 Introduction

Microscopy—both in its two-dimensional (2D) or three-dimensional (3D) variants—requires generation and variation of contrast, often enabled by chemical staining or labeling. Classical histology and histo-pathology of thin tissue sections relies on a portfolio of established staining agents, such as H&E (hematoxylin and eosin) to name the most common example. Suitable stains exhibit preferential binding to different cellular organelles and biomolecular constituents, such as nuclei, extracellular matrix, and cytoplasm. Specific antibody labels create exclusive contrast for desired target proteins. Highest sensitivity down to single molecule level is enabled by optical fluorescence techniques, including the super-resolution microscopy techniques, such as stimulated emission depletion microscopy (STED), photo-activated localization microscopy (PALM) or stochastic optical reconstruction microscopy (STORM)[1] for which specific dyes were developed.[2] Larger penetration depth and field of view (FOV) in particular for the investigation of tissues are offered by light-sheet microscopy,[3] again relying on stains or specific labels. Electron microscopy (EM) of biological tissue also takes advantage of well established heavy metal stains, notably by the classical protocols based on osmium tetroxide (OsO_4), uranyl acetate ($UO_2(CH_3COO)_2$), or lead citrate $C_{12}H_{10}O_{14}Pb_3$. More recent developments, such as rOTO,[4] are instrumental for labeling brain tissue[4,5] in view of connectivity studies. This has, for example, enabled high resolution reconstruction of neuronal networks of mouse retina.[6] 3D tissue imaging by EM is enabled by serial block-face electron microscopy or focused ion beam scanning electron microscopy but is still very limited in volume throughput, and depending on volume size can take several days to weeks, strongly restricting the feasibility of high-throughput comparative studies. Sample preparation and staining pre- or post-sectioning can take days and require a lot of experience and manual processing of the sample.

Phase-contrast X-ray computed tomography (XPCT) based on image formation by free space propagation complements optical and EM techniques. It covers an intermediate resolution range from several microns down to the range of 10 nm and offers high bulk penetration and volume throughput. In addition, XPCT can be implemented in multi-scale approach, covering larger tissue scales up to the entire organ level. XPCT has even been implemented for *in-vivo* imaging of free breathing mice[7] and can quantify morphology and cytoarchitecture of biological tissue.[8–10] Different pathologies of the central nervous system (CNS), such as, e.g., Alzheimer[11] or multiple sclerosis,[12] have been addressed by virtual histology based on XPCT. The acquired volumes can be analyzed by advanced statistical methods, for example, based on optical transport theory,[13] machine learning algorithms,[14] or shape measure analysis.[9,15] Importantly, XPCT has been introduced for unstained tissues, including formaldehyde-fixed paraffin embedded tissue blocks, fully compatible with clinical pathology.[8,16]

Notwithstanding the benefits of unstained preparations and 3D imaging of electron density without additives, it is evident that contrast variation based on stains or labels is an asset that should also be exploited in XPCT. In this way, structural features that are visible in synchrotron radiation (SR) can be contrasted also in instruments with much lower partial coherence,[17,18] or individual neurons can be contrasted with respect to the tissue background, for example, by the Golgi-Cox staining protocol.[19] To this end, radiocontrast agents are used,[20] which increase X-ray attenuation by accumulating heavy atoms with high atomic number Z at different tissue sites. Well known examples are barium-, lead-, or iodine-based agents, phosphotungstic acid, and gold nanoparticles to mention a few. Radiocontrast agents are rarely optimized for XPCT but are typically translated either from clinical radiology and hence optimized for absorption contrast or from EM, again strongly inclined toward absorption. Instead, one would seek a balance between increase of phase shift while keeping absorption tolerable, depending on the specific application. Since phase shift is proportional to the projected electron density, a heavy atom contrast agent is both an enhancer for attenuation as well as for the phase signal. In terms of atomic form factors $Z + f'(E) + if''(E)$ describing the atomic interaction with X-rays of photon energy E, for a stain optimized for phase instead of absorption contrast, one would prefer atomic labels, which are located in the upper right corner of a plane spanned by the axis $Z + f'$ and $(Z + f')/f''$. This is because labels with high $Z + f'$ values warrant high contrast, which is desired, but at the price of poor phase retrieval if f'' becomes too high. Note that for given concentrations, this choice of atomic form factors directly translates to high δ and high δ/β ratio. For the typical photon energy range 5 to 50 keV where XPCT by free space propagation is

Downloaded From: https://www.spiedigitallibrary.org/journals/Journal-of-Medical-Imaging on 11 Jan 2024
Terms of Use: https://www.spiedigitallibrary.org/terms-of-use

performed, one may search within a surprisingly large range $24 \leq Z \leq 64$, in order to be well above the corresponding L-edges and below the K-edge (in order to keep f'' reasonable). This would exclude commonly used radiocontrast agents W, Os, Pb, or U, at least for bulk labeling. Note that iodine based stains[21] as well as recently developed *Br* based eosin stains for the cellular cytoplasm[22] meet this criterion, whereas the Pb based hematein stain targeting cellular nuclei[23] would hence not fall into this category.

Interestingly, several stains that have recently been proposed in EM as replacements of commonly used highly toxic or radioactive labels, such as osmium tetroxide (OsO_4) or uranyl acetate (UAc), may be interesting candidates for XPCT. Notably, a few years ago UranyLess was developed as a safe and non-radioactive stain while providing many of the other characteristics of UAc.[24] Most recently, neodymium acetate (NdAc) was proposed as another substitute and was used to replace UAc in several routine applications.[25] Belonging to the same side group in the periodic table, oxidation states and chemical properties are similar, but at the same time a higher $(Z + f')/f''$ ratio compared to UAc is reached. Note that for the same number density of atoms, this equally corresponds to an increase in the δ/β ratio, where $n = 1 - \delta + i\beta$ denotes the X-ray index of refraction.

Here, we study the suitability of NdAc for XPCT. Intact murine eyes as well as other parts of the CNS were prepared and stained with NdAc as well as alternative stains. We compare the imaging results qualitatively and quantitatively and evaluate the suitability of NdAc for high resolution XPCT. Inline with the ubiquitous assumption of a homogeneous object, we reconstruct the XPCT data based on a fixed coupling of β and δ. This parameter is selected by varying this parameter in the reconstruction, around the calculated values (for the assumed elemental composition).

Murine eyes were selected as test samples since they allow easy penetration of the stains and consist of multiple tissue layers as well as the retina, with all structures showing different chemical compositions and therefore different binding affinities. In previous studies, mammalian and insect eyes were proven to be suitable objects to be investigated by XPCT.[26,27] Also, there are indications that neurodegenerative diseases are preceded by degeneration of the retinal structure, making it an important object to study the origins and progression of conditions, such as Parkinson's disease[28] or Alzheimer's.[29] The retina consists of the following layers (optical nerve side to eyeball): choroid, retinal pigmented epithelium, layer of rods and cones, outer nuclear layer, outer plexiform layer, inner nuclear layer, inner plexiform layer, Ganglion cell layer, nerve fiber layer, and the internal limiting membrane where the incident light falls in.

Hence, the main goal of the this paper is to investigate the potential benefit of using NdAc as a contrast agent in XPCT by evaluating its optical properties and by comparing it to OsO_4 and iodine stained murine eyes samples. The paper starts with the description of the staining and embedding procedure (Sec. 2.1) and is complemented with a brief outline of the tomography setups, namely the commercial laboratory instrument equipped with a nano-focus source (Sec. 2.2), and the custom built synchrotron holo-tomography endstation GINIX at beamline P10 of PETRA III storage ring (DESY, Hamburg) in Sec. 2.3. The results achieved with the two setups are subsequently presented in Secs. 3.1 and 3.2. Finally, the staining results are quantified and evaluated in Sec. 3.3, tomographic reconstructions are visualized by 3D renderings. The work closes with a discussion of the results and a brief outlook in Sec. 4.

2 Methods

2.1 Staining and Embedding Procedure

Murine CNS tissues from previously dissected laboratory mice (75d old, C57N/Bl6 mice, sacrificed for a different biomedical research project) were used to showcase and compare the staining agents of interest here. The effective uptake of OsO_4 by various retinal layers was already demonstrated in a preceding high resolution XPCT study.[30] Besides fully intact eyes, tissue from murine cerebellum and corpus callosum was collected to investigate the binding behavior of the different staining agents, namely OsO_4, Lugol's iodine solution (LIS), and NdAc.

The mice were perfused or immersion-fixed with a K+S solution. After several washing steps in 0.1 M phosphate buffer (PB) (3×15 min), the tissue (diameter ~ 1.5 mm) was post-fixated with 2% OsO_4 at 4°C (4 h). To this end, 4% OsO_4 stock solution was mixed in

Downloaded From: https://www.spiedigitallibrary.org/journals/Journal-of-Medical-Imaging on 11 Jan 2024
Terms of Use: https://www.spiedigitallibrary.org/terms-of-use

a 1:1 ratio with 0.2M PB. In the next step, the tissue was repeatedly washed (3×15 min) in the same buffer and dehydrated with increasing concentration of acetone (1 h) and embedded by infiltration with 2:1 acetone/EPON (1.5 h), 1:1 acetone (1.5 h), 1:2 acetone/EPON (overnight), and pure EPON (4 h).[31] Finally, the samples were mounted in polyimide (Kapton) tubes and polymerized for 24 h at 60°C. Staining with OsO_4, LIS, and NdAc was conducted in the same way. The staining protocols for OsO_4 and LIS are already well established in X-ray tomography and proved to enhance contrast by binding to different regions of biological tissue.[21,32]

Since Nd and U belong to the same side group of the periodic table, similar chemical properties with regard to binding and clustering at different regions is expected and can indeed be observed, see for example Fig. 1(c). In buffer, Nd is present as a trivalent cation that accumulates preferentially at anionic groups, in particular phosphate groups in nucleic acids, phosphate, and carboxyl groups, such as gangliosides, mostly present on cell surfaces.[33] NdAc is applied in aqueous solution (4%) to give sufficient contrast, which could be further enhanced by a higher NdAc concentration or, e.g., a replacement of water by a saturated methanolic solution.[34] In contrast to UAc, NdAc is neither radioactive nor highly toxic, significantly facilitating the handling and staining procedure.

2.2 Laboratory Nano-CT Imaging

While synchrotron imaging is still regarded as the gold standard in XPCT, state-of-the-art laboratory sources can provide sufficient flux and coherence for in-house (phase-contrast) tomography with voxel sizes in the range of a few microns down to the sub-micron range. Recent results have opened up a promising approach to study biological tissues in the laboratory[18,35,36] and to translate 3D virtual histology from synchrotron to compact laboratory sources, important for pre-clinical and clinical research.

While the tissue samples have been scanned at several different custom built in-house CT instruments, we here present results obtained at the commercially available EasyTom nano-CT system (RX Solutions, France). The system allows for switching detectors and sources and

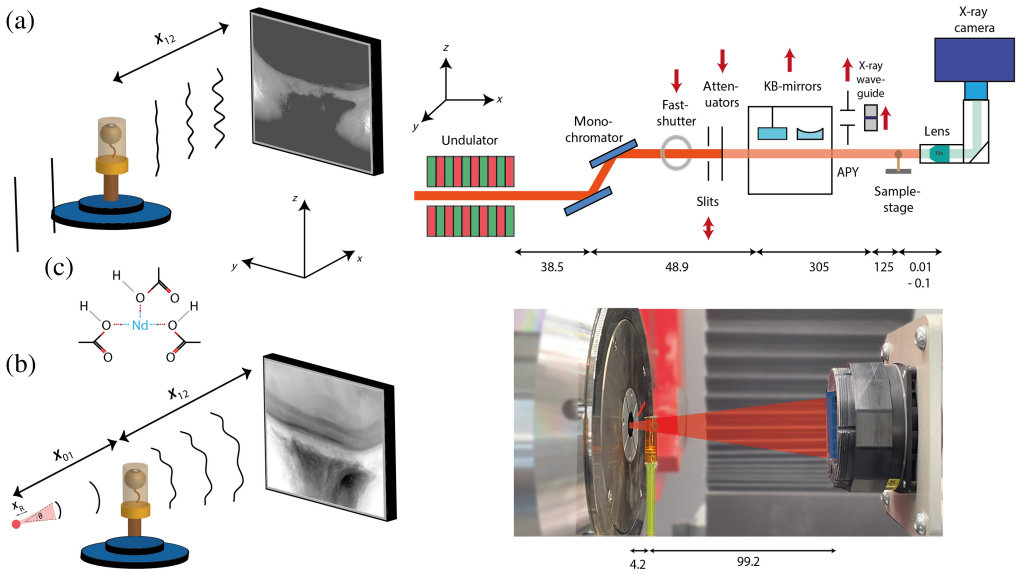

Fig. 1 (a) Schematic overview of the parallel beam setup at the GINIX endstation with an attenuator in and KB-mirrors and X-ray waveguide out of the beam path (right). The propagated exit wave of a given sample projection impinges on the detector at a distance x_{12} behind the sample, chosen to reach the holographic regime (left). (b) Laboratory nano-CT imaging setup with opening angle θ, a spatial coherence length $\xi_{\perp}$. The ratio of source-to-sample (x_{01}) and sample-to-detector (x_{12}) distance (left) defines the magnification $[(x_{01} + x_{12})/x_{01}]$. Photo of laboratory setup (right): sample holder (green), beam (red), and detector area (blue). (c) 2D chemical structure of NdAc. A trivalent cation is coordinated by three acetate molecules that are formed by combination of acetic acid with a base. All lengths are in mm.

Downloaded From: https://www.spiedigitallibrary.org/journals/Journal-of-Medical-Imaging on 11 Jan 2024
Terms of Use: https://www.spiedigitallibrary.org/terms-of-use

Table 1 Parameters of tomographic scans for stain comparison at laboratory source.

	Unstained eye	OsO_4 eye (1 h)	NdAc eye	NdAc CC	NdAc cerebellum
Energy (keV)	80	80	80	80	80
Detector type	CCD	CCD	CCD	CCD	CCD
Exposure time (s)	2.5	2.5	2.5	2	2
# Acc	12	12	12	6	6
FOV (px)	1983×1224	1983×1224	1983×1224	1983×1226	1986×1231
Voxel size (μm)	0.73	0.73	0.73	0.79	2
x_{01} (mm)	4.2	4.2	4.2	4.5	12.1
x_{02} (mm)	103.4	103.4	103.4	103.4	108.4

flexible adjustment of geometry and source parameters well suited to optimize the setting for a specific application. In the present case, the nano-CT source was used with a LaB6 cathode and a transmission anode with an adjustable spot size (0.4 to 1.5 μm), a CCD camera (Gadox scintillator with free fiber optics coupling, 9 μm pixel pitch, and 2016×1344 pixel after 2×2 binning), and a custom-made sample holder. High geometric magnification was selected by moving the sample close to the source spot Fig. 1(b). $N_{\mathrm{prj}} = 1568$ images were recorded over 360 deg with a tube voltage of 80 keV and a polychromatic spectrum. Accumulation of several images at the same position was used to improve the signal-to-noise ratio (SNR). Before the scan, the reference images at selected angles were recorded for subsequent tracking and correction of spot size movement over the duration of the scan. Flat field images were recorded inside the EPON material to receive normalized intensities in the projection images by correction for low-frequency effects.[37] The exact settings are given in Table 1.

After the scan was completed, the reference images were used to account for source spot movement, and the rotation axis was corrected. Finally, ring filter correction and phase retrieval algorithm were applied before the actual tomographic reconstruction. For phase reconstruction, a Paganin-based phase retrieval algorithm was used and the according parameter (δ/β) was set manually.[38] Fiji[39] and MATLAB (R2020a) were used for further analysis and NVIDIA IndeX[40] for rendering of the volumes. Video 1 shows an entire rendered optical nerve with retina scanned at the laboratory setup (Avizo, Thermo Fisher Scientific, Germany).

2.3 Synchrotron-Based X-Ray Tomography

SR sources provide users with highly brilliant and coherent X-ray beams that allow one to exploit quantitative phase contrast on multiple scales and correspondingly different geometries. In this experiment, the parallel beam tomography setup[41] of the GINIX endstation[42] at the P10 beamline of the PETRA III storage ring (DESY, Hamburg) was used. Due to the high number of photons, a continuous rotation and short exposure time is sufficient to fill the dynamic range of a 16-bit detector, resulting in reduced moving artifacts and a short overall scan time (≈ 2 min). For the present measurements, single-distance tomograms with 3000 projections over 360 deg were recorded. The monochromaticity (Si(111) channel-cut monochromator) allows the tissue to be studied at a well defined photon energy instead of the broad bandpass unavoidable for in-house CT. The sample's optical indices and imaging parameters fall within the regime where CTF-based phase retrieval is suitable to solve the phase problem.[43]

For the setup, the sCMOS camera pco.edge 5.5 (PCO, Germany) with a 100 Hz maximum frame rate, 2560×2160 pixel, a rolling shutter, and a fast scan mode was mounted on an high resolution detection system (Optique Peter, France) with a 50 mm-thick LuAG:Ce scintillator and a 10× magnifying microscope objective.[41] This resulted in an effective pixel size of 0.65 μm and a total exposure time of about 75 s. Focusing optics such as KB-mirrors or waveguides as well as the fastshutter were moved out of the beam path, whereas the beam size was adjusted by an upstream slit system resulting in a beam size of about 2 mm × 2 mm [Fig. 1(a)].

Downloaded From: https://www.spiedigitallibrary.org/journals/Journal-of-Medical-Imaging on 11 Jan 2024
Terms of Use: https://www.spiedigitallibrary.org/terms-of-use

With a sample-to-detector distance (SDD) of 149 mm, the holographic regime was reached with a Fresnel number of

$$F = \frac{px_{\text{eff}}^2}{x_{12}\lambda} \approx 0.0366, \tag{1}$$

for $E = 16$ keV, wavelength λ, and an effective pixel size px_{eff} of 0.65 μm. Phase reconstruction was carried out using the linearized single step CTF-approach,[43,44] which is implemented in our code package HoloTomoToolbox.[45]

Tomographic reconstruction was carried out after flat- and dark field correction with the *iradon* function implemented in MATLAB using a Ram-Lak filter for backprojection. To avoid ring artifacts, hot pixel in the projections was removed by replacing them with the mean of adjacent pixel. The Fresnel number was verified and if needed refined by inspecting the radially averaged PSF of a hologram to the expected CTF and according re-scaling. In addition, a wavelet-based filtering approach was applied to further mitigate ring artifacts occurring during the reconstruction.[46] For post processing and visualization, the Fiji software was used.

3 Results

3.1 Laboratory Comparison

3.1.1 *Murine eye imaging*

We first present in-house scans of EPON embedded murine eyes, stained either with NdAc or OsO_4 as well as an unstained reference sample, see Fig. 2(a). Already based on visual inspection of the projection images, which were recorded with the exact same settings (Table 1), clear differences between the samples can be observed. While the unstained tissue shows a general lack of contrast, which is reflected by a very low SNR in the reconstructed images, different regions of the retina are contrasted and emphasized in the stained preparations. The projections of the NdAc treated retina show mainly the surfaces/interfaces of the tissue to be contrasted, whereas OsO_4 seems to reach a higher and more bulk-like penetration and binding, resulting in a more uniform and stronger attenuation in all regions. A qualitative analysis of the intensity profiles across the retinal layers in OsO_4 and NdAc stained layers indicates larger deviations of attenuation values depending on the according layer, thus suggesting a higher specificity of the NdAc stain. In addition, different retinal layers show higher absorption properties. While, e.g., in the OsO_4 stained sample mostly the choroid layer is strongly targeted, the NdAc shows a high binding affinity to the sclera, the internal limiting membrane as well as rods and cones in the retina. In addition, cells in the Ganglion cell layer are highlighted and their distribution can be investigated. We also note that the NdAc stained region seems to be slightly compressed in comparison to the OsO_4 stained sample ($\approx 60\mu$m thinner), which might be attributed to the selection of the compared slices as well as to sample preparation artifacts or differences in specimens.

3.1.2 *Murine brain imaging*

Murine corpus callosum and cerebellum were also imaged in the laboratory setup to investigate the binding behavior of NdAc in different neuronal tissues (Fig. 3; Table 1). It can be observed that in both cases, surfaces and interfaces are pronounced, possibly because these interfaces are defined by well exposed cell surfaces with anionic phospholipids. Also, vasculature seems to be affected by the stain and the whole vascular network becomes easily distinguishable from the surrounding tissue, which opens up a promising approach for rendering and segmentation of the vascular tree. In the cerebellum, gray matter is also clearly separable from white matter. Cell layers on the other hand could not be clearly be resolved. This could be explained based on insufficient sampling and resolution, or—more likely—by a lack of contrast, which could either result from a low penetration depth of the stain, the compactness, and higher tissue density, or to the lower binding of Nd in these regions.

Downloaded From: https://www.spiedigitallibrary.org/journals/Journal-of-Medical-Imaging on 11 Jan 2024
Terms of Use: https://www.spiedigitallibrary.org/terms-of-use

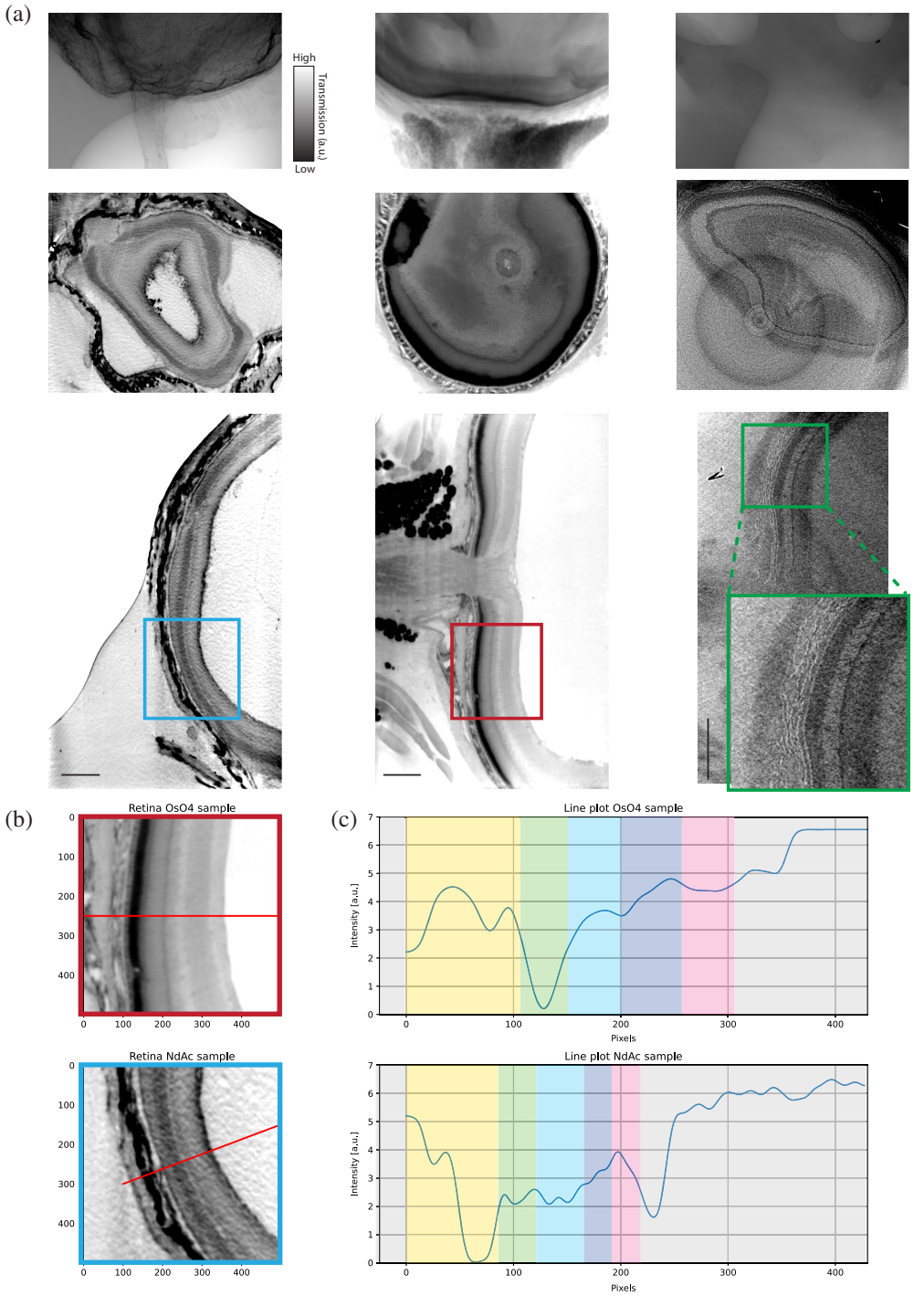

Fig. 2 Comparison between NdAc (left), OsO_4 (center), and unstained (right) entire murine eye samples by in-house nano-CT system. (a) First row shows a projection image of each dataset. The second row depicts a selected slice from the *xy*-plane (maximum intensity projections over five slices) and the third row from the *yz*-plane. In (b) and (c), smoothed line profiles from a similar region in the OsO_4 and NdAc sample are plotted. Each colored region represents a layer of the murine eye. Yellow, sclera; green, choroid; light blue, rods and cones layer; dark blue, nuclear/plexiform layers; pink, ganglion cell layer. Scan settings and reconstruction parameters are given in Table 1. Scale bars: 200 μm.

Downloaded From: https://www.spiedigitallibrary.org/journals/Journal-of-Medical-Imaging on 11 Jan 2024
Terms of Use: https://www.spiedigitallibrary.org/terms-of-use

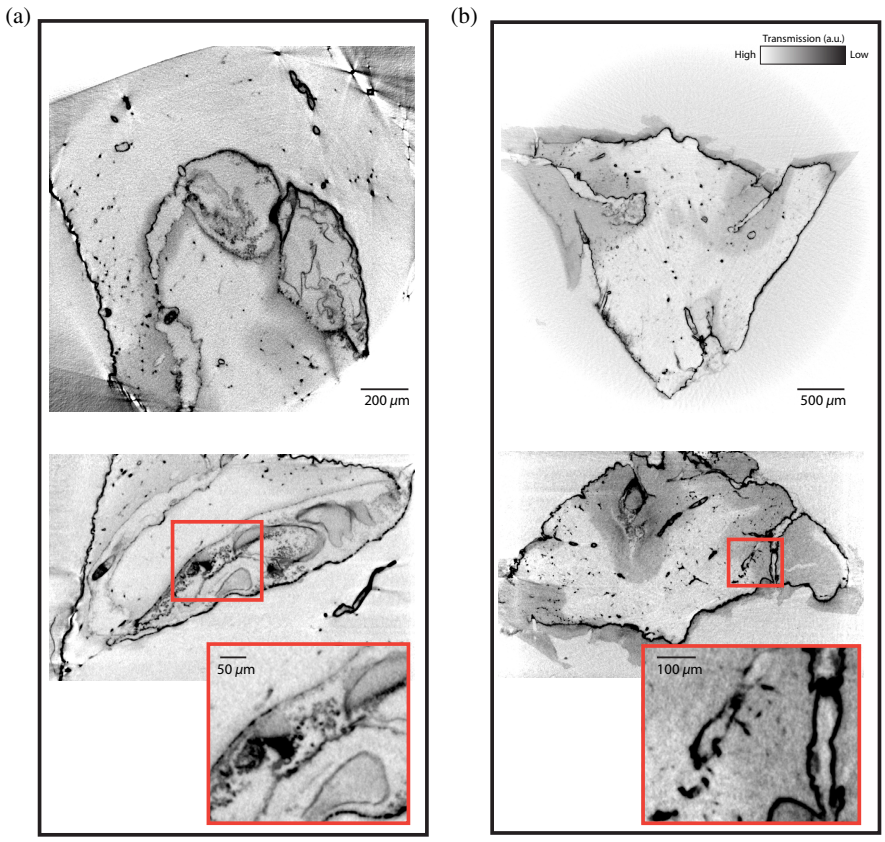

Fig. 3 (a) Corpus callosum and (b) cerebellum stained with NdAc shown in *xy*-plane (top) and *xz*-plane (bottom), both as maximum intensity projections over five slices, recorded with the laboratory setup. Scan settings and reconstruction parameters are listed in Table 1.

3.2 Qualitative Comparison of Different Staining Agents Using Synchrotron Phase-Contrast CT

Synchrotron data were collected from a NdAc, OsO_4, Lugol's solution stained retina, and compared with an unstained sample at 13.8, 16, and 20 keV. In Fig. 4, reconstructed slices are presented for all samples scanned at 16 keV since this photon energy yielded the most comparable results.

Here, our previous assumptions following the qualitative assessment of the laboratory scans can be confirmed, however, now at much increased resolution and contrast. NdAc seems to significantly enhance contrast of cones and rods as well as the sclera and the Ganglion cell layer while OsO_4 and LIS target the choroid. While cones and rods also seem to be targeted by the stains, OsO_4 lacks any specificity and increases the attenuation in the sample uniformly, with the heavy osmium atoms causing a strong attenuation of photons in the tissue. LIS on the other hand is very favorably binding to the choroid, decreasing the number of photons passing through the sample, thus decreasing the SNR, while other layers of interest in the retina seem to only experience a minor increase in contrast. It is worth noticing that OsO_4, which is known to strongly bind to lipids, yields strong contrast for adipose tissue and eye muscles right behind the eyeball, allowing for an easy segmentation and detailed investigation of these structures [Fig. 5(b)].

3.3 Quantification of Staining Results

Tomography with monochromatic SR allows to draw quantitative conclusions on the composition when modeling the absorption coefficients and/or the reconstructed phase shifts based on atomic form factors. Since the phase retrieval scheme used here yields images of coupled phase and absorption contrast based on its homogeneous object approximation, it is per se not straightforward to extract the local concentration of the stain, i.e., a spatially varying stochiometry. However, in propagation based XPCT, the contrast of the low spatial frequencies is dominated

Downloaded From: https://www.spiedigitallibrary.org/journals/Journal-of-Medical-Imaging on 11 Jan 2024
Terms of Use: https://www.spiedigitallibrary.org/terms-of-use

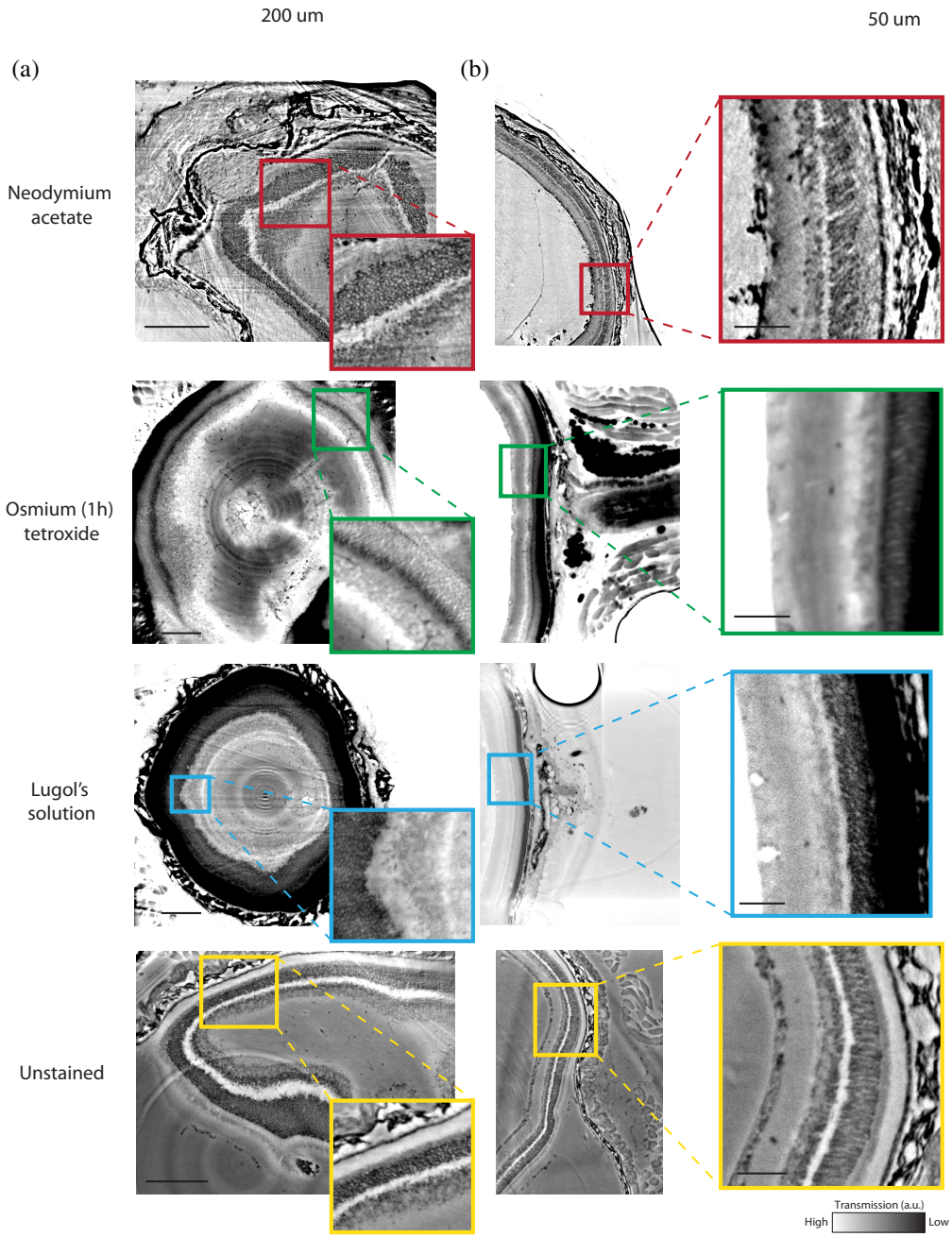

Fig. 4 Comparison between NdAc, OsO_4, LIS stained and unstained entire murine eye samples scanned in parallel beam geometry at 16 keV at the synchrotron facility (SDD: 149 mm). (a) A selected slice from the *xy*-plane (scale bar: 200 μm) and (b) a slice from the *yz*-plane with a zoomed section (scale bar: 50 μm). Scan settings and reconstruction parameters are given in Table 2.

by absorption. Therefore, we can artificially generate a "pure" absorption image by local averaging the projections such that the phase effect cancels out. This is done only for the purpose of quantifying the local concentration in a coarse-grained sense, see the corresponding workflow shown in Fig. 6(c). The reconstructed absorption coefficients in the reconstruction volume are then compared between a NdAc stained sample and an unstained sample, see Fig. 6(b), scanned both at 13.8 and 16 keV. To this end, the projections are filtered, e.g., with a median filter (8×8 pixel), allowing one to take only the attenuation into consideration. A comparable region of interest involving the retinal layers with 400×400 pixel (16 keV) is then cropped from a reconstructed slice. Histograms of the gray values are shown in Fig. 6(d). By subtraction of the

Downloaded From: https://www.spiedigitallibrary.org/journals/Journal-of-Medical-Imaging on 11 Jan 2024
Terms of Use: https://www.spiedigitallibrary.org/terms-of-use

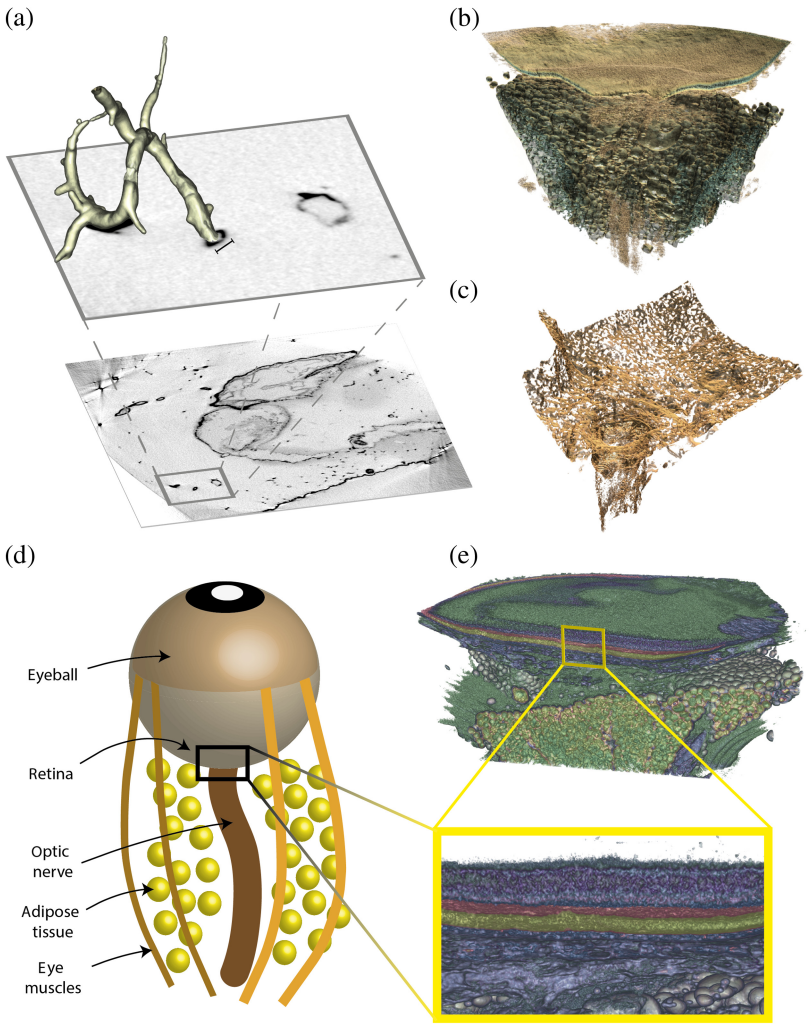

Fig. 5 Rendering with NVIDIA IndeX. (a) A part of a vascular tree extracted from a NdAc stained murine corpus callosum [see Fig. 3(a)]. Scale bar: 40 μm. (b) An OsO_4 stained rendered eye sample, where the adipose tissue and eye muscles are clearly visible (green), whereas the optical nerve is indicated and culminates into the retinal layer (turquoise). (c) An NdAc stained rendered eye sample where the sclera, coating the optic nerve, is clearly visible and extends into the grid-like, stiff collagenous structure. (b) and (c) were recorded at the laboratory nano-CT source. (d) An illustration of the eye structure and (e) The retinal layers of the OsO_4 stained eye [same sample as in (b)].

Table 2 Parameters of synchrotron measurements of different stains with a parallel beam setup.

	Unstained	OsO_4 (1h)	Lugol	NdAc
Energy (keV)	13.8 and 16	16 and 20	13.8 and 16	13.8 and 16 and 20
Exposure time (ms)	35	35	35	35
FOV (mm)	1.6×1.4	1.6×1.4	1.6×1.4	1.6×1.4
Voxel size (nm)	650	650	650	650
SDD (mm)	29 and 149	29 and 149	29 and 149	29 and 149
Phase retrieval	CTF	CTF	CTF	CTF
δ/β (@ 16 keV)	35	10	35	5

Downloaded From: https://www.spiedigitallibrary.org/journals/Journal-of-Medical-Imaging on 11 Jan 2024
Terms of Use: https://www.spiedigitallibrary.org/terms-of-use

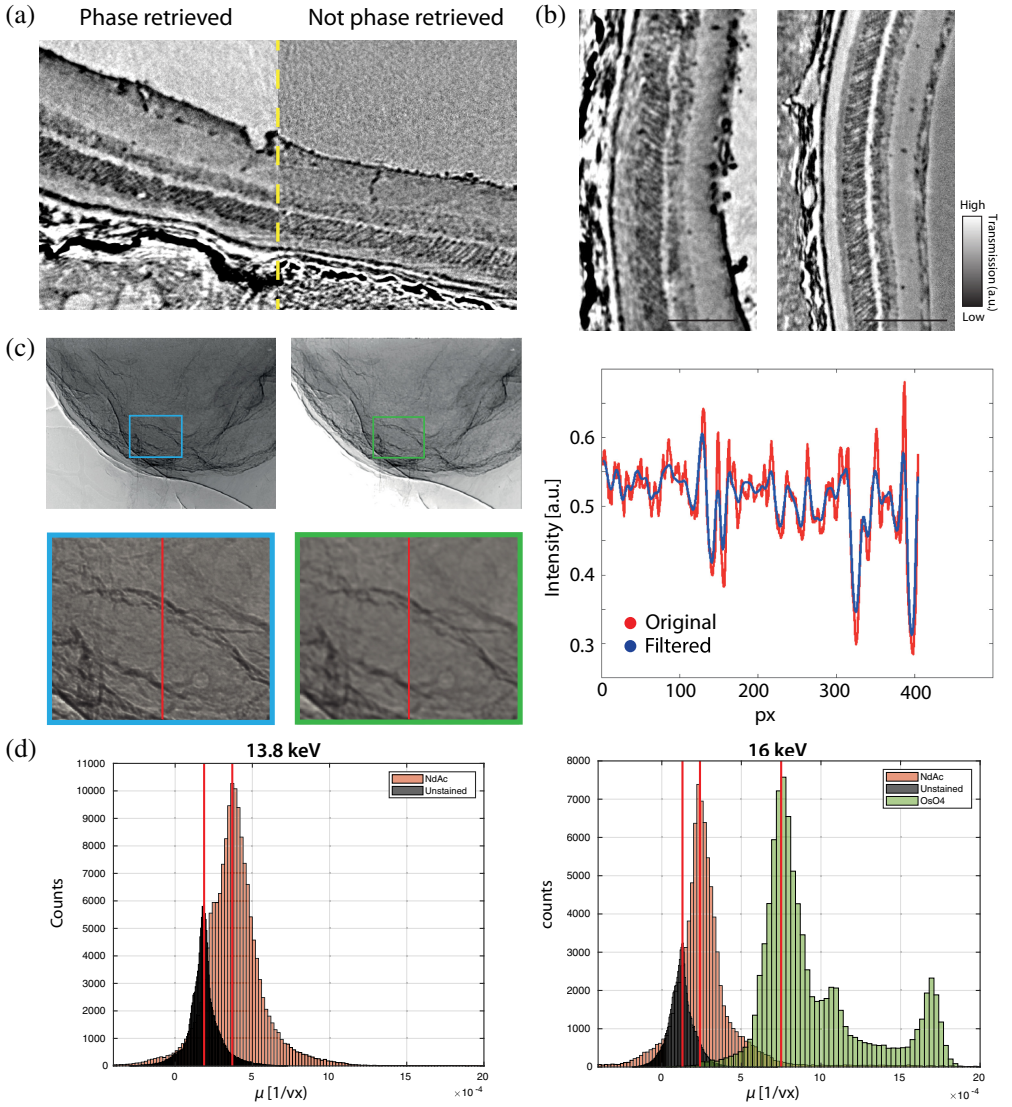

Fig. 6 Quantitative analysis of the NdAc staining from synchrotron measurements. (a) Reconstructed slice (left) with and (right) without phase retrieval, demonstrating the benefit of phase retrieval for the image quality and quantitative contrast. The example shows NdAc stained retinal layers recorded with the synchrotron setup. (b) Qualitative comparison between NdAc stained (left) and unstained retina (right) at 13.8 keV. Scale bar: 100 μm. (c) Illustration of the workflow associated with suppressing the phase effects by local averaging of the projection (left) to create an absorption-dominated image (center). The line plot (right) shows the corresponding reduction of edge enhancement. (d) Attenuation per voxel shown for similar region of NdAc, OsO_4, and unstained samples in histograms for 13.8 and 16 keV. The red lines mark the attenuation value where the number of counts peaks. By subtraction from the unstained peak, the attenuation of NdAc and OsO_4 is determined.

attenuation peaks, we obtain the additional attenuation coefficients (or more precisely the histogram thereof) attributed to NdAc in units $(1/vx)$, allowing us to effectively isolate the staining component from the tissue and to infer its atomic density based on the known atomic form factor (f'' component).

The refractive index

$$n = 1 - \delta + i\beta \tag{2}$$

shows a dependence of the dispersion term δ and the imaginary part

$$\beta = \frac{r_0 \lambda^2}{2\pi} \rho_a f''(\omega), \tag{3}$$

Downloaded From: https://www.spiedigitallibrary.org/journals/Journal-of-Medical-Imaging on 11 Jan 2024
Terms of Use: https://www.spiedigitallibrary.org/terms-of-use

where $r_0 = 2.82 \cdot 10^{-15}$ m denotes the Thomson scattering length, ρ_a is the number density of atoms, λ is the photon's wavelength, and $f'(\omega)$ is the atomic scattering factor and real part of the correction derived from the Kramers–Konig relation. The linear attenuation coefficient is related to β as

$$\mu = \frac{4\pi\beta}{\lambda} \tag{4}$$

and is directly measured by the number of photons reaching the detector.

Substituting Eq. (4) into Eq. (3), we obtain an atomic mass density of

$$\rho_a = \frac{\mu}{2r_0\lambda f''(\omega)}. \tag{5}$$

Since we know λ ($\lambda[\text{Å}] = 12.938/\text{E[keV]}$), the number density and subsequently the mass density ($\rho = \rho_a A/N_A$) with the known atomic mass A and the Avogadro constant N_A can be calculated. The atomic scattering factors f' and f' for uranium, osmium, and NdAc are plotted in Fig. 7, where the absorption edges (L, M) are indicated. To investigate their optical properties in regard to the relationship between absorption and refraction, the δ/β ratio is calculated as[47]

$$\delta/\beta = \frac{Z + f'}{f''}. \tag{6}$$

From the plots, a significantly higher ratio can be inferred for neodymium at energies above 17 keV and between 2.5 and 6 keV, where therefore an advantage of neodymium can be expected for phase contrast imaging compared to uranium.

At 13.8 keV, the difference of the attenuation peaks was determined as $1.8250 \cdot 10^{-4}(1/\text{vox})$. Substituting this into Eq. (5), an approximate number density for NdAc of $0.0117(\text{Nd}/\text{nm}^3)$ is obtained. To check consistency, the procedure was repeated for samples scanned at 16 keV, yielding a number density of $0.0105(\text{Nd}/\text{nm}^3)$. In contrast, OsO_4 shows a difference in attenuation peaks from the unstained sample of about $6.2 \cdot 10^{-4}(1/\text{vox})$ resulting in an estimated number

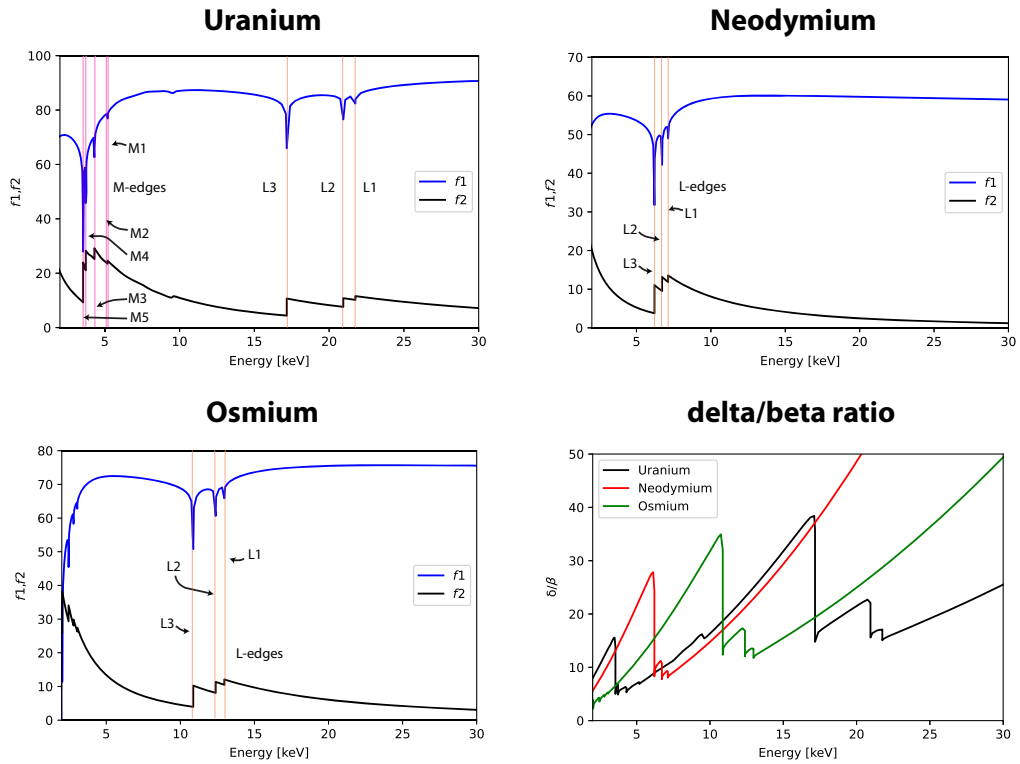

Fig. 7 Plots of atomic scattering factors f' and f'' for uranium, neodymium, and osmium (with denoted M- and L-edges) and their energy-dependent δ/β ratios [Eq. (6)].

Downloaded From: https://www.spiedigitallibrary.org/journals/Journal-of-Medical-Imaging on 11 Jan 2024
Terms of Use: https://www.spiedigitallibrary.org/terms-of-use

Table 3 Number densities and estimated mean distance between Nd atoms for different energies.

	NdAc (13.8 keV)	NdAc (16 keV)	OsO_4 (16 keV)
Number density (Nd/nm^3)	0.0117	0.0105	0.0249
Mean distance (nm)	2.73	2.83	2.13

density of $0.0249(\mathrm{Nd}/\mathrm{nm}^3)$. Number densities and estimated free distances between atoms are listed in Table 3.

4 Discussion

The results indicate NdAc to be a promising stain for XPCT, which is much better suited for phase contrast than, for example, UAc, based on the different X-ray optical properties resulting from the lower atomic number, in particular its higher δ/β ratio. At the same time, the binding properties are similar to those known for UAc, e.g., preferential binding to anionic groups such as phosphate and carboxyl groups at cell surfaces, based on the triple valency of the Nd^{3+} cation. Note that NdAc is an anionic salt with a solubility of 7.77 mol/L. From the strong non-linear electrostatics expected for a triple valency, one may expect that a particularly strong interaction may take place with anionic lipids, such as phosphatidylserine, which in neuronal cells, however, is mainly located in the cytosolic leaflet of the plasma membrane, and hence not easily accessible. It remains elusive to us why the strong contrast for the endothelium is observed, which, however, makes NdAc particularly promising for studies of the vasculature in neuronal tissue. In the murine eye, NdAc also seems to be targeting rods and cones in the retina as well as the Ganglion cell layer and in particular sclera. In comparison to OsO_4, we observe a stronger nuance and selectivity when it comes to stain deposition and targeting of some tissue structures, providing the opportunity to study these structures in more detail without over-contrasting. Atom density estimates based on the analysis of the absorption coefficients should be further refined in subsequent work to draw conclusion about the selective partitioning into different tissue regions and the amount of stain deposited in a certain voxel. At the same time, NdAc solutions could be tested in controlled *in vitro* suspension by small-angle X-ray scattering to probe the interaction with selected lipids or biomolecular structures in quantitative terms. From the present work, we can also infer that the number density of NdAc is considerably smaller than that of OsO_4. Importantly, its larger δ/β-values for a wide range of photon energies, making it a promising candidate stain for XPCT. Note, however, that at the resolution tested, the main advantage of the stained versus unstained samples derived from the fact that the stain opens up new imaging opportunities for laboratory instruments. Contrarily, SR already gave very convincing image quality also for unstained samples. To this end, high resolution/high magnification in the holo-tomography regime would be an interesting next step.

In summary, we could show that NdAc penetrates the sample uniformly and can increase contrast and resolution at the CNS cyto-architectural level, at least for some targets and for laboratory instruments. While there is an overall superior image quality at laboratory sources, it still remains to be clarified, how to interpret the binding and staining patterns, for example, by further correlative imaging with conventional histology. Note that the present example of murine retina in whole-eye preparations is only a very specific example, which needs to be complemented by a wider range of tissues. Due to its more favorable optical constants, NdAc is more compatible with most X-ray phase-retrieval approaches than most other EM heavy metal stains and can thus help to translate synchrotron quality to the laboratory.

4.1 Animal Welfare

Mice were housed in the mouse facility of the Max Planck Institute of Experimental Medicine with controlled ventilation (inward airflow, exhaust to the outside), temperature ($21 \pm 2^{\circ}$C) and controlled rel. humidity ($55\% \pm 10\%$) in individually ventilated cages. Mice were group-housed 3 to 5 mice per cage in a 12-h dark/light cycle with ad libitum access to food and water. For the

Downloaded From: https://www.spiedigitallibrary.org/journals/Journal-of-Medical-Imaging on 11 Jan 2024
Terms of Use: https://www.spiedigitallibrary.org/terms-of-use

procedure of sacrificing vertebrates for subsequent preparation of tissue, all regulations given in the German animal welfare law (TierSchG §4) are followed.

5 Appendix: Supporting Information

Video 1. Osmium tetroxide stained whole eye sample recorded with in-house nano-CT system. (MPG, 52.6 MB [URL: https://doi.org/10.1117/1.JMI.10.5.056001.s1]).

Disclosures

An earlier version of this work was presented at SPIE Optics and Photonics 2022 as contribution 12242-3 "Neodymium acetate as a contrast agent for X-ray phase-contrast tomography" (presentation date: August 22, 2022). It was published in the corresponding conference proceedings (SPIE Optics and Photonics 2022: Developments in X-Ray Tomography XIV).[48] Apart from that, there are no relevant financial interests in the paper and no other potential conflicts of interest to disclose.

Code, Data, and Materials Availability

CT-reconstruction data, measurement settings and analysis scripts have been deposited in GRO.data (DOI: https://doi.org/10.25625/ZOHHEI). All study data are available upon request.

Acknowledgments

This paper was funded by the Deutsche Forschungsgemeinschaft (DFG, German Research Foundation)—Project-ID 432680300 – SFB 1456 and EXC 2067/1-390729940. We thank Markus Osterhoff for integration of cameras and beamline control tools and Michael Sprung and Fabian Westermeier for excellent working conditions at beamline P10. We also acknowledge assistance in visualization with NVIDIA IndeX (NVIDIA Corporation, USA). An earlier version of this work was also presented at SPIE Optics and Photonics 2022 and is published in the corresponding conference proceedings (SPIE Optics and Photonics 2022: Developments in X-Ray Tomography XIV).

References

1. K. Prakash et al., "Super-resolution microscopy: a brief history and new avenues," *Philos. Trans. R. Soc. A: Math. Phys. Eng. Sci.* **380**, 20210110 (2022).
2. M. V. Sednev, V. N. Belov, and S. W. Hell, "Fluorescent dyes with large Stokes shifts for super-resolution optical microscopy of biological objects: a review," *Methods Appl. Fluoresc.* **3**, 042004 (2015).
3. Y. Wan, K. McDole, and P. J. Keller, "Light-sheet microscopy and its potential for understanding developmental processes," *Annu. Rev. Cell Dev. Biol.* **35**, 655–681 (2019).
4. Y. Hua, P. Laserstein, and M. Helmstaedter, "Large-volume en-bloc staining for electron microscopy-based connectomics," *Nat. Commun.* **6**, 7923 (2015).
5. S. Mikula and W. Denk, "High-resolution whole-brain staining for electron microscopic circuit reconstruction," *Nat. Methods* **12**, 541–546 (2015).
6. M. Helmstaedter et al., "Connectomic reconstruction of the inner plexiform layer in the mouse retina," *Nature* **500**, 168–174 (2013).
7. K. Shaker et al., "Phase-contrast X-ray tomography resolves the terminal bronchioles in free-breathing mice," *Commun. Phys.* **4**, 249 (2021).
8. M. Töpperwien et al., "Three-dimensional virtual histology of human cerebellum by X-ray phase-contrast tomography," *Proc. Natl. Acad. Sci. U. S. A.* **115**, 6940–6945 (2018).
9. M. Reichardt et al., "3D virtual histopathology of cardiac tissue from Covid-19 patients based on phase-contrast X-ray tomography," *eLife* **10**, e71359 (2021).
10. J. Reichmann et al., "Human lung virtual histology by multi-scale X-ray phase-contrast computed tomography," *Phys. Med. Biol.* **68**, 115014 (2023).
11. M. Chourrout et al., "Brain virtual histology with X-ray phase-contrast tomography Part II: 3D morphologies of amyloid-beta plaques in Alzheimer's disease models," *Biomed. Opt. Express* **13**, 1640–1653 (2021).
12. A. Cedola et al., "X-ray phase contrast tomography reveals early vascular alterations and neuronal loss in a multiple sclerosis model," *Sci. Rep.* **7**, 5890 (2017).
13. M. Eckermann et al., "Three-dimensional virtual histology of the human hippocampus based on phase-contrast computed tomography," *Proc. Natl. Acad. Sci. U S A* **118**(48), e2113835118 (2021).
14. J. Stroebel et al., "Convolutional neuronal networks combined with X-ray phase-contrast imaging for a fast and observer-independent discrimination of cartilage and liver diseases stages," *Sci. Rep.* **10**, 20007 (2020).

Downloaded From: https://www.spiedigitallibrary.org/journals/Journal-of-Medical-Imaging on 11 Jan 2024
Terms of Use: https://www.spiedigitallibrary.org/terms-of-use

15. P. M. Jensen et al., "Zonohedral approximation of spherical structuring element for volumetric morphology," *Lect. Notes Comput. Sci.* **11482**, 128–139 (2019).
16. A. Khimchenko et al., "Extending two-dimensional histology into the third dimension through conventional micro computed tomography," *NeuroImage* **139**, 26–36 (2016).
17. M. Eckermann et al., "Three-dimensional virtual histology of the cerebral cortex based on phase-contrast X-ray tomography," *Biomed. Opt. Express* **12**, 7582–7598 (2021).
18. M. Eckermann et al., "Phase-contrast X-ray tomography of neuronal tissue at laboratory sources with sub-micron resolution," *Proc. SPIE* **11112**, 111120R (2019).
19. M. Töpperwien et al., "Phase-contrast tomography of neuronal tissues: from laboratory- to high resolution synchrotron CT," *Proc. SPIE* **9967**, 99670T (2016).
20. Y. C. Dong and D. P. Cormode, *17 Heavy Elements for X-Ray Contrast*, pp. 457–484, De Gruyter (2021).
21. P. M. Gignac et al., "Diffusible iodine-based contrast-enhanced computed tomography (diceCT): an emerging tool for rapid, high-resolution, 3-D imaging of metazoan soft tissues," *J. Anat.* **228**(6), 889–909 (2016).
22. M. Busse et al., "3D-non-destructive imaging through heavy-metal eosin salt contrast agents," *Chem. – Eur. J.* **27**(14), 4561–4566 (2021).
23. M. Müller et al., "Nucleus-specific X-ray stain for 3D virtual histology," *Sci. Rep.* **8**, 17855 (2018).
24. N. Benmeradi, B. Payre, and S. L. Goodman, "Easier and safer biological staining: high contrast uranyless staining of TEM grids using mPrep/g capsules," *Microsc. Microanal.* **21**, 721–722 (2015).
25. J. Kuipers and B. N. G. Giepmans, "Neodymium as an alternative contrast for uranium in electron microscopy," *Histochem. Cell Biol.* **153**, 271–277 (2020).
26. J. Romell et al., "Laboratory phase-contrast nanotomography of unstained Bombus terrestris compound eyes," *J. Microsc.* **283**, 29–40 (2021).
27. Y. Ivanishko et al., "Feasibility study of the 3D visualization at high resolution of intra-cranial rabbit eyes with X-ray CT phase-contrast imaging," *Invest. Ophthalmol. Vision Sci.* **58**, 5941–5948 (2017).
28. Y. Zhang et al., "Retinal degeneration: a window to understand the origin and progression of Parkinson's disease?" *Front. Neurosci.* **15**, 799526 (2022).
29. A. Ashok et al., "Retinal degeneration and Alzheimer's disease: an evolving link," *Int. J. Mol. Sci.* **21**, 7290 (2020).
30. M. Töpperwien, *3d Virtual Histology of Neuronal Tissue by Propagation-Based X-Ray Phase-Contrast Tomography*, Göttingen Series in X-Ray Physics, Göttingen University Press, Göttingen (2018).
31. W. Möbius et al., "Chapter 20. Electron microscopy of the mouse central nervous system," *Methods Cell Biol.* **96**, 475–512 (2010).
32. M. Bartels et al., "Myelinated mouse nerves studied by X-ray phase contrast zoom tomography," *J. Struct. Biol.* **192**, 561–568 (2015).
33. M. A. Hayat, *Principles and Techniques of Electron Microscopy: Biological Applications*, Cambridge University Press, Cambridge, UK, New York (2000).
34. K. S. Suvarna, C. Layton, and J. D. Bancroft, *Bancroft's Theory and Practice of Histological Techniques E-Book*, Elsevier Health Sciences (2012).
35. L. Massimi et al., "Exploring Alzheimer's disease mouse brain through X-ray phase contrast tomography: from the cell to the organ," *NeuroImage* **184**, 490–495 (2019).
36. L. Massimi et al., "Detection of involved margins in breast specimens with X-ray phase-contrast computed tomography," *Sci. Rep.* **11**, 3663 (2021).
37. C. L. Walsh et al., "Imaging intact human organs with local resolution of cellular structures using hierarchical phase-contrast tomography," *Nat. Methods* **18**, 1532–1541 (2021).
38. D. Paganin and K. A. Nugent, "Noninterferometric phase imaging with partially coherent light," *Phys. Rev. Lett.* **80**, 2586–2589 (1998).
39. J. Schindelin et al., "Fiji: an open-source platform for biological-image analysis," *Nat. Methods* **9**, 676–682 (2012).
40. E. Schneider et al., "NVIDIA IndeX accelerated computing for visualizing Cholla's galactic winds," *Parallel Comput.* **107**, 102809 (2021).
41. J. Frohn et al., "3D virtual histology of human pancreatic tissue by multiscale phase-contrast X-ray tomography," *J. Synchrotron. Radiat.* **27**, 1707–1719 (2020).
42. T. Salditt et al., "Compound focusing mirror and X-ray waveguide optics for coherent imaging and nano-diffraction," *J. Synchrotron. Radiat.* **22**, 867–878 (2015).
43. P. Cloetens et al., "Holotomography: quantitative phase tomography with micrometer resolution using hard synchrotron radiation x rays," *Appl. Phys. Lett.* **75**, 2912–2914 (1999).
44. M. Krenkel et al., "Phase-contrast zoom tomography reveals precise locations of macrophages in mouse lungs," *Sci. Rep.* **5**, 9973 (2015).
45. L. Lohse et al., "A phase-retrieval toolbox for X-ray holography and tomography," *J. Synchrotron. Radiat.* **27**, 852–859 (2020).

Downloaded From: https://www.spiedigitallibrary.org/journals/Journal-of-Medical-Imaging on 11 Jan 2024
Terms of Use: https://www.spiedigitallibrary.org/terms-of-use

46. B. Münch et al., "Stripe and ring artifact removal with combined wavelet—Fourier filtering," *Opt. Express* **17**, 8567 (2009).
47. T. Salditt, T. Aspelmeier, and S. Aeffner, *Biomedical Imaging*, De Gruyter (2017).
48. J. Reichmann et al., "Neodymium acetate as a contrast agent for X-ray phase-contrast tomography," *Proc. SPIE* **12242**, 1224204 (2022).

Jakob Reichmann is a PhD student at the University of Göttingen. He received his bachelor's degree in physics from the Ludwigs-Maximilian University of Munich and a double-MS degree from the Technical University of Munich and Royal Institute of Technology (KTH). He is interested in biomedical applications, development of novel methods, and quantitative analysis techniques for X-ray phase-contrast tomography. He is a member of SPIE.

Torben Ruhwedel is a technician responsible for running facility EM projects at the Electron Microscopy Facility at the Max Planck Institute for Multidisciplinary Sciences-City Campus. His experience includes various techniques for cell biology and biomaterials such as high pressure freezing (HPF), TEM, SEM, and 3D volume EM.

Wiebke Möbius studied biology at the University of Göttingen and Bonn (Germany) and received her diploma in 1994. She received her PhD from the University of Bonn in 1998 by investigating the intracellular transport of glycosphingolipids by electron microscopy. She then worked as a postdoctoral researcher in Utrecht (The Netherlands) in the group of Prof. Geuze and Slot until 2003. She spent another year as postdoctoral researcher at the EMBL (Heidelberg, Germany) before she moved to Göttingen in 2004 to take over the Electron Microscopy Facility of the Max-Planck-Institute of Experimental Medicine, which changed to the Max-Planck-Institute for Multidisciplinary Sciences in 2022. She works at the City Campus as a research associate studying myelin biology.

Tim Salditt is a professor of experimental physics at the Institute for X-ray Physics of the University of Göttingen. He studied physics in Munich and Grenoble and received his PhD in 1995 for work on non-specular X-ray reflectivity. After research in membrane biophysics using scattering techniques, he started to work on coherent diffractive imaging in order to extend X-ray structure analysis of biological samples with real-space resolution. He has developed X-ray waveguide optics for nanoscale holographic imaging and tomography and more recently got involved in the translation of phase contrast tomography from synchrotron to laboratory instrumentation. He has been spokesperson of the collaborative research center Nanoscale Photonic Imaging for 12 years and is a principle investigator of the DFG Center for Excellence Multi-Scale Bioimaging. He is a member of the Academy of Sciences in Göttingen and of the DESY scientific advisory committee.

Downloaded From: https://www.spiedigitallibrary.org/journals/Journal-of-Medical-Imaging on 11 Jan 2024
Terms of Use: https://www.spiedigitallibrary.org/terms-of-use